

# JGR Space Physics

## RESEARCH ARTICLE

10.1029/2021JA029880

### Key Points:

- We use the BAFIM-ELSPEX analysis combination to calculate the energy spectra of precipitating electrons with high time resolution
- Using the fitted electron density data in precipitation events leads to wider energy spectra, and larger auroral power and field-aligned current estimates
- Auroral power calculated using the BAFIM-ELSPEX analysis correlates well with the 427.8 nm emission line intensity

### Supporting Information:

Supporting Information may be found in the online version of this article.

### Correspondence to:

H. W. Tesfaw,  
Habtamu.Tesfaw@oulu.fi

### Citation:

Tesfaw, H. W., Virtanen, I. I., Aikio, A. T., Nel, A., Kosch, M., & Ogawa, Y. (2022). Precipitating electron energy spectra and auroral power estimation by incoherent scatter radar with high temporal resolution. *Journal of Geophysical Research: Space Physics*, 127, e2021JA029880. <https://doi.org/10.1029/2021JA029880>

Received 12 AUG 2021  
Accepted 11 MAR 2022

© 2022 The Authors.

This is an open access article under the terms of the [Creative Commons Attribution-NonCommercial License](#), which permits use, distribution and reproduction in any medium, provided the original work is properly cited and is not used for commercial purposes.

## Precipitating Electron Energy Spectra and Auroral Power Estimation by Incoherent Scatter Radar With High Temporal Resolution

Habtamu W. Tesfaw<sup>1</sup> , Ilkka I. Virtanen<sup>1</sup> , Anita T. Aikio<sup>1</sup> , Amoré Nel<sup>2</sup> , Michael Kosch<sup>2,3,4</sup> , and Yasunobu Ogawa<sup>5</sup> 

<sup>1</sup>Space Physics and Astronomy Research Unit, University of Oulu, Oulu, Finland, <sup>2</sup>South African National Space Agency, Hermanus, South Africa, <sup>3</sup>Department of Physics, Lancaster University, Lancaster, UK, <sup>4</sup>Department of Physics and Astrophysics, University of Western Cape, Bellville, South Africa, <sup>5</sup>National Institute of Polar Research, Tokyo, Japan

**Abstract** This study presents an improved method to estimate differential energy flux, auroral power and field-aligned current of electron precipitation from incoherent scatter radar data. The method is based on a newly developed data analysis technique that uses Bayesian filtering to fit altitude profiles of electron density, electron temperature, and ion temperature to observed incoherent scatter spectra with high time and range resolutions. The electron energy spectra are inverted from the electron density profiles. Previous high-time resolution fits have relied on the raw electron density, which is calculated from the backscattered power assuming that the ion and electron temperatures are equal. The improved technique is applied to one auroral event measured by the EISCAT UHF radar and it is demonstrated that the effect of electron heating on electron energy spectra, auroral power, and upward field-aligned current can be significant at times. Using the fitted electron densities instead of the raw ones may lead to wider electron energy spectra and auroral power up to 75% larger. The largest differences take place for precipitation that produces enhanced electron heating in the upper E region, and in this study correspond to fluxes of electrons with peak energies from 3 to 5 keV. Finally, the auroral power estimates are verified by comparison to the 427.8 nm auroral emission intensity, which shows good correlation. The improved method makes it possible to calculate unbiased estimates of electron energy spectra with high time resolution and thereby to study rapidly varying aurora.

## 1. Introduction

Electron precipitation to the high-latitude ionosphere is a key process in magnetosphere-ionosphere coupling and in the physics of the mesosphere-lower thermosphere region, because the precipitating electrons carry electric current, transfer energy from the magnetosphere to the ionosphere, ionize neutral atoms and molecules, cause optical auroral emissions, heat the electron gas, and change the ion composition. High-resolution observations are needed in studies of these phenomena, as the processes often take place in small spatial and temporal scales.

Electron precipitation is quantitatively characterized by the energy distribution of the primary electrons. Electron acceleration processes in the magnetosphere that lead to different energy spectral shapes are discussed by Dombeck et al. (2018) and Newell et al. (2009). For a known differential energy flux, altitude profiles of ion production rate and auroral emission rates can be determined if the neutral atmospheric parameters are known (Fang et al., 2010; Rees, 1963).

Indirect estimation of the differential energy flux from electron density altitude profiles observed with an incoherent scatter radar (ISR) is an efficient way to observe electron precipitation from ground (Brekke et al., 1989; Kaeppler et al., 2015; Kirkwood, 1988; Semeter & Kamalabadi, 2005; Simon Wedlund et al., 2013; Virtanen et al., 2018; Vondrak & Baron, 1977). Unlike in situ observations with fast-moving satellites and rockets, the radar observations allow one to follow the time evolution of the electron precipitation along the local geomagnetic field.

Two different analysis techniques are commonly used to obtain electron densities from an ISR observation. Scaling the backscattered power with radar system parameters results in the so-called raw electron density ( $N_r$ ), which is equal to the actual electron density ( $N_e$ ) if electron and ion temperatures are equal. A more sophisticated way is to make a least squares fit of a parametric incoherent scatter spectrum model to the observed spectra. Typically,

electron density ( $N_e$ ), electron temperature ( $T_e$ ), ion temperature ( $T_i$ ), and line-of-sight ion bulk velocity ( $V_i$ ) are fitted.

The electron density profiles need to be observed with high-resolutions in range and time to enable accurate estimation of the rapidly varying electron energy spectra. While plasma parameter fits to EISCAT ISR data are typically made with a few kilometer range resolution and some tens of seconds time resolution using the Grand Unified Incoherent Scatter Design and Analysis Package (GUISDAP; Lehtinen & Huuskonen, 1996), the electron energy spectra fits require range resolution better than 2 km (Semeter & Kamalabadi, 2005) and time resolution of the order of five seconds (Virtanen et al., 2018).

Since other high-latitude ISR facilities cannot produce better resolutions either, previous high time resolution energy spectrum fits have been based on raw electron densities (Burns et al., 1990; Dahlgren et al., 2011; Lanchester et al., 1994, 1996, 1997; Semeter & Kamalabadi, 2005; Virtanen et al., 2018), while the fitted electron densities have been used with 1 min or coarser resolutions (Fujii et al., 1995; Hargreaves & Devlin, 1990; Kaeppler et al., 2015; Kirkwood & Eliasson, 1990; Kosch et al., 2001; Osepian & Kirkwood, 1996; Strickland et al., 1994). However, the electron precipitation tends to heat the electron gas, which makes the implicit assumption of  $T_e = T_i$  questionable in calculation of  $N_r$ . The raw density  $N_r$  is smaller than the actual density  $N_e$  if  $T_e > T_i$ , which may lead to underestimation of the precipitating energy flux if  $N_r$  is used in electron energy spectrum fits.

An optical signature of the electron precipitation are auroral emissions, which are produced when excited atoms, molecules, and ions return to their ground states. Optical observations are vital to complement the radar observations and to put them into wider context. While optical observations lack the altitude information provided by radars, they can image the auroral emissions in 2D and can reach angular and time resolutions superior to those of the radars. Energy flux of the precipitating electrons can also be inferred from the auroral blue line (427.8 nm) emission intensity which is emitted by relaxation of excited  $N_2^+$  molecular ions. Previous studies have shown direct proportionality between line of sight integrated blue line emission intensity and total energy flux of the precipitating electrons (Omholt, 1971; Partamies et al., 2004; Rees & Luckey, 1974; Strickland et al., 1989).

The 427.8 nm emission intensity and auroral power inverted from radar data showed good correlation in a study by Kaeppler et al. (2015), who used fitted electron density data with 4.5 km range, and 1 and 3 min time resolutions. The coarse resolutions were justified since the authors concentrated on stable auroral features. To study dynamic small-scale structures with sub-second resolution, raw electron density profiles were combined with optical observations by Lanchester et al. (1997). They found a good correlation between the radar and optical data when fields of view of both instruments were uniformly filled with the observed aurora. Large fluxes found in their event were within extremely narrow features that did not fill the fields of view of the instruments, making the comparison at these scales complex. More recently, Tuttle et al. (2014) reported underestimation of energy flux estimated from radar data when an auroral feature narrower than the radar beam was observed.

The aim of this study is to introduce an improved method to calculate energy spectra of auroral electrons from ISR measurements with high time resolution. We perform full four-parameter fits to the observed incoherent scatter spectra with high-resolutions in time and range and use the actual fitted  $N_e$  in high-resolution electron energy spectrum inversion for the first time. Using the fitted electron density in the inversion removes a bias in the fitted energy spectra that occurs during electron heating events if the raw electron density is used.

The high-resolution plasma parameter fit is possible with the newly developed Bayesian Filtering Module (BAFIM; Virtanen et al., 2021). BAFIM makes use of smoothness priors in time and range (along the geomagnetic field line) for the plasma temperature profiles to reach high-resolution in the electron density fits, as described in Section 4.1. Electron energy spectra are then inverted from the BAFIM-fitted electron density profiles using a method developed by Virtanen et al. (2018) known as ELSPEC (ELectron SPECtrum) and described in Section 4.3. ELSPEC uses parametric models for the electron energy spectra, models the ion production and loss rates, and solves the electron density as function of time from its continuity equation. Difference between the modeled electron density profile and the radar observation is then iteratively minimized to find the best matching electron energy spectra.

The BAFIM-ELSPEC analysis combination is applied to an auroral event that comprises wide range of auroral features. By comparing the ELSPEC analysis results obtained from the fitted and raw electron densities, we study the effects of enhanced electron heating on the calculated energy spectra of the precipitating electrons.

To validate our auroral power estimates, we compare the auroral power (total energy flux) calculated from the BAFIM-ELSPEC analysis combination with that of the 427.8 nm spectral (blue) line emission intensity.

The article is organized as follows; data and measurements are introduced in Section 2, the auroral event is described in Section 3, the radar data analysis and the effect of electron heating are discussed in Section 4, and auroral power derived from the radar observations is compared to optical observations in Section 5. Discussion and summary are presented in Section 6.

## 2. Data and Measurements

The active auroral event presented in this study took place on 9 March 2016, 19:40–23:40 UT over Tromsø, Norway. The EISCAT UHF radar near Tromsø (69.58°N, 19.23°E Geodetic, and 66.67°N, 101.41°E Geomagnetic) was pointed along the local geomagnetic field and it was running the “arc1” experiment, which uses a 64-bit alternating code sequence (Lehtinen & Häggström, 1987) with 6  $\mu$ s bit length. The 128 pulses of the code sequence were transmitted with 3.468 ms inter-pulse periods, and autocorrelation function (ACF) data decoded to 900 m range resolution were stored from each 443.9 ms long pulse sequence. In this study, we use data integrated to 4 s time resolution.

In addition to the ISR observations, we characterize the dynamics of the observed auroral structures using all-sky camera (ASC) and narrow field of view (FoV) optical observations. All-sky images of the auroral green line emission (557.7 nm) with 1 s time resolution are obtained from the Watec monochromatic imager (WMI; Ogawa et al., 2020) located at the EISCAT Tromsø radar site. In addition, we use an EMCCD imager located at the radar site (Nel et al., 2021) for narrow FoV observations of small-scale auroral structures around and within the radar beam. The detector images auroral emissions at wavelength 427.8 nm with a 30° FoV and 3 s exposure time. The camera system was pointing to the geomagnetic zenith.

Local and global (Nose et al., 2015) auroral electrojet indices are also used to monitor the geomagnetic activity. Geomagnetic field data obtained from the IMAGE network of magnetometers are used to derive the local auroral electrojet (IL) index (Kallio et al., 2000). Finally, an induction coil magnetometer at Kilpisjärvi (69.06°N, 20.77°E Geodetic, and 66.07°N, 102.30°E Geomagnetic) is used to monitor the geomagnetic pulsation activity (Raita & University of Oulu, 2022).

## 3. Event Description

Overview of the event is given in Figure 1. A time-lapse video of the ASC and narrow FoV auroral images is provided as a Supporting Information S1. The raw electron density obtained from the EISCAT UHF radar observation is placed in the first panel of the figure. Keograms produced from the North-South cut of the narrow FoV and ASC auroral images over the radar zenith are shown in the second and third panels, respectively. We make coordinate transformation at 110 km to calculate the latitudes for the keograms. The horizontal white lines in the keograms represent position of the radar beam. Power spectra of geomagnetic pulsations, and local (IL) and global (AL) auroral electrojet indices are shown in the fourth and fifth panels, respectively. Selected all-sky auroral images are shown in Figure 2. Magnetic midnight at Tromsø is at about 21:30 UT.

At 19:30 UT there were several faint arcs in the FoV of the ASC which later drifted equatorward. After few minutes, at about 19:39 UT, the first signature of an intensification of an arc is seen in the eastern horizon. At about the same time, the peak frequency in the pulsation power spectrum jumps from below 1 mHz to about 0.5 Hz, which indicates development of PiB pulsations (McPherron, 2005; Olson, 1999). PiB pulsation development and sudden brightening of auroral arcs are typical indicators of substorm activation (Mishin et al., 2020; Sakurai & Saito, 1976). The IL and AL indices decrease abruptly at about 19:40, which is another indication of substorm onset (Hsu & McPherron, 2012; Tanskanen, 2009).

Based on the AL index, three relatively small substorm onsets took place during the studied time interval with rough onset times at 19:40, 21:30, and 22:40 UT. During the first substorm, the IL index remained much smaller than the AL index indicating that the substorm onset region was not in Scandinavia, but rather to the east, closer to magnetic midnight.

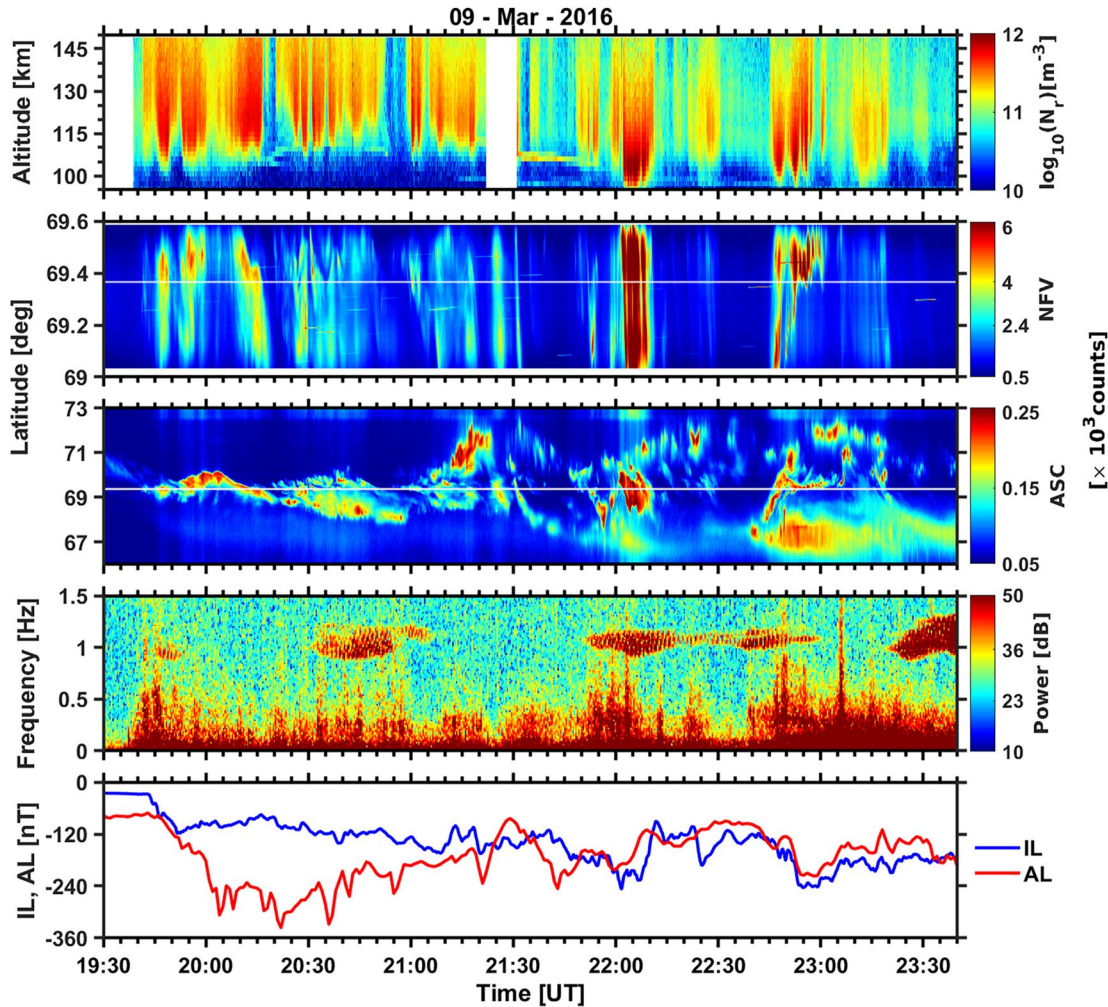


**Figure 1.** An overview of the auroral event. Panels from top to bottom: raw electron density, narrow FoV keogram (427.8 nm), all-sky camera (ASC) Keogram (557.7 nm), geomagnetic pulsation spectrogram, and IL and AL electrojet indices.

In addition to the continuous PiB activity, magnetic pulsations show signatures of Pc1 pulsations near 1 Hz, which are produced by protons injected to the inner magnetosphere and interacting with ion cyclotron waves (Saito, 1969). It is probable that this injection is a consequence of substorm onset.

The radar starts recording large ionization enhancements after 19:44 UT when the auroral arcs in the vicinity of the radar beam start to intensify. The radar beam was inside a broad luminous region with multiple bright arcs until 19:51 UT, as shown in auroral images A and B of Figure 2, and the radar observes the first period of enhanced ionization between 19:44 and 19:51 UT. Intensity of the arcs in the radar beam then fade, and by 19:52 UT they are substituted by several east-west aligned arcs forming together a bright bulge that expands poleward. Selected images of the bulge are shown in panels C and D of Figure 2.

Probing the poleward advancing bulge, the radar measures an ionization enhancement between 19:52 and 20:00 UT. The bulge leaves the radar beam at about 20:01 UT and continues expanding poleward until 20:04 UT. Then it starts to retreat from its poleward extent and advances equatorward across the radar beam. As indicated in auroral images E and F of Figure 2, the radar was observing the equatorward moving arc between 20:07 and 20:16 UT to produce the third ionization enhancement. The east-west aligned arc continued drifting equatorward and left the radar beam at about 20:16:30 UT.

At about 20:22 UT, the AL index attained its minimum value of about  $-350$  nT, indicating the end of the first substorm expansion phase. During the first substorm recovery phase, between 20:20 and 21:30, multiple auroral



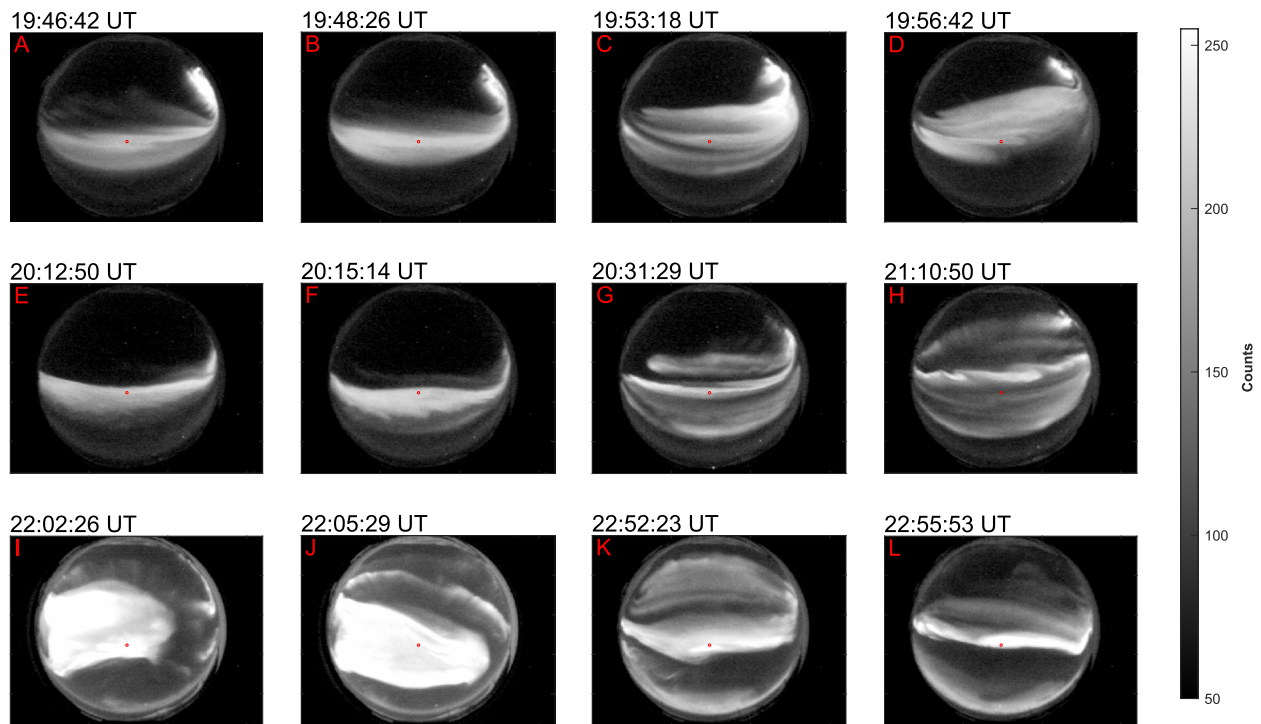


**Figure 2.** Selected auroral images taken from the ASC camera observation on 9 March 2016. The radar beam is shown as a red dot in the images. North is up and east is to the right.

features with folds and curls are created across the auroral oval as shown in the ASC and narrow FoV keograms in Figure 1. Sample auroral images taken from this time interval are shown in panels G and H of Figure 2. When these auroral structures perform radar beam crossings, series of several short-lived ionization enhancements are produced between 20:20 and 21:20 UT.

During the first substorm, all the arcs were streaming mostly toward the west. Counter-streaming arcs were also observed so that in the northern part the streaming was to the east and in the southern part toward the west, indicating converging electric field structure and auroral potential drop above the ionosphere (Aikio et al., 2002; Carlson et al., 1998). We also find the energy spectra of the electron flux corresponding to these arcs to be in the form of inverted-V type structures.

Following break up of the second substorm at about 21:30 UT, a bright auroral feature is seen in the north-west horizon of the ASC at about 21:35 UT, indicating the onset region of this substorm was to the west of Tromsø. After the onset, the streaming inside the arcs becomes mainly eastward. Eventually, a bright auroral bulge, expanding to the ASC FoV from the west, is formed at about 21:57 UT. Selected images of the bulge are shown in panels I and J of Figure 2. When the bulge passes through the radar beam at about 21:59, it produces an electron density enhancement characterized by largest peak electron densities (in the order of  $10^{12} \text{ m}^{-3}$ ) and lowest peak altitudes (about 100 km) of the event. The narrow FoV and ASC keograms show that the radar beam was at the center of this intensifying bulge from 22:00 until 22:11 UT. The auroral bulge fades in its intensity by 22:12. After that and until 22:40 several auroral features with varying luminosity are observed across the horizon of the ASC.

The AL index shows that onset of the third substorm occurs at about 22:40 UT. Indeed, at 22:39 UT an auroral arc was observed intensifying from west to east in the very southern horizon of the ASC, indicating the onset was to the west of Scandinavia. Auroral images K and L of Figure 2 show that the radar measured the last ionization enhancement between 22:44 and 22:56 UT when these auroral arcs drift poleward. ASC and narrow FoV keograms indicate that the radar was observing the equatorward edge of an east-west aligned auroral arc between 22:53 and 22:56 UT.

In addition to ionization by precipitating electrons, sporadic E layers can be seen during two time intervals in the electron density plot. The first sporadic E layer is observed between 20:20 and 20:52 UT in the altitude regions of 109 km, and the second one is between 21:30 and 21:48 UT at about 106 km.

#### 4. Electron Energy Spectrum Analysis

The analysis method we use to calculate the differential electron energy flux from the EISCAT UHF ISR data consists of two steps. First, plasma parameters are fitted to the incoherent scatter data with high time and range resolutions using the combination of GUIDAP (Lehtinen & Huuskonen, 1996) and BAFIM (Virtanen et al., 2021). Second, the fitted electron density altitude profiles are inverted into differential energy fluxes of precipitating electrons using the ELSPEC software (Virtanen et al., 2018). In this section, we introduce the analysis methods and address the effect of electron heating on the raw electron density  $N_r$  for the first substorm discussed in Section 3. We consider both the bias in raw electron density and its effects on the electron energy spectrum fits.

##### 4.1. Fitted and Raw Electron Densities

In the traditional “gated” incoherent scatter plasma parameter fits, one averages the incoherent scatter ACF over selected intervals in range and time, and fits the plasma parameters to the averaged ACFs in each range-gate and time-step. Each fit is independent of the others and one cannot include prior information about shape of the plasma parameter profiles, or about their expected temporal variations. Statistical accuracy of the fitted plasma parameters depends on the resolutions, since accuracy of the observed ACF is improved with increasing integration in time or range. The standard GUIDAP analysis of EISCAT radar data uses the gated analysis principle. Accuracy of the GUIDAP fit results depends also on the level of ionization in the observed region, which affects the signal-to-noise ratio. Although E region electron density is typically high during active aurora, resolutions needed to follow the associated rapid variations in electron energy spectra are practically out of reach of the standard four-parameter fits of  $N_e$ ,  $T_e$ ,  $T_i$ , and  $V_i$  with GUIDAP.

Due to the limitations of the four-parameter fits, the high-resolution electron density observations are typically based on the raw electron density, which is the backscattered signal power multiplied with radar system parameters. Assuming that the Debye length is much smaller than the radar wavelength, which is a well-justified assumption in E region observations with the EISCAT UHF radar, the relation between the raw density  $N_r$  and the actual density  $N_e$  can be written as (Baron, 1977; Semeter & Kamalabadi, 2005):

$$N_r = \frac{2N_e}{(1 + T_r)}, \quad (1)$$

where  $T_r = T_e/T_i$ . Obviously,  $N_e = N_r$  when  $T_r = 1$ , but  $N_e > N_r$  when  $T_r > 1$ . For example,  $N_e = 1.5 \cdot N_r$  if  $T_r = 2$ , which is not an unusual temperature ratio in the upper E region during electron precipitation. Auroral events with enhanced E region electron temperature have been investigated for example, by Wickwar et al. (1981), who found that the electron density altitude profiles calculated with correct temperature ratio have lower peak altitudes and greater peak electron densities than those of the raw electron density altitude profiles.

An alternative to the gated analysis is the full-profile analysis (Holt et al., 1992; Hysell et al., 2008; Lehtinen et al., 1996), in which one fits full range-profiles of plasma parameters. The full-profile analysis allows one to include prior information about the plasma parameter profiles, but it is also computationally heavier than the gated analysis. The BAFIM (Virtanen et al., 2021) is an extension module to GUIDAP, which allows one to include prior information about plasma parameter gradients in both range and time in the gated GUIDAP analysis. BAFIM thus extends the idea of full profile analysis to smoothness in both range and time, but without increasing the computational burden of the gated analysis. BAFIM introduces correlations in between adjacent range-gates and time-steps in a way that leads to effectively coarser resolutions in range and time than those defined by the range-gates and time-steps. Since the correlations are defined for each plasma parameter separately, one can use effectively coarser resolutions for  $T_e$ ,  $T_i$ , and  $V_i$ , but fit the electron density  $N_e$  with the best possible resolution. The assumption of smoothness in the  $T_e$  and  $T_i$  profiles is justified in field-aligned observations, because the high mobility along the magnetic field prevents generation of large field-aligned temperature gradients in the upper E and lower F regions.

#### 4.2. High-Resolution Plasma Parameter Fit With BAFIM

For this study, we ran a BAFIM fit of  $N_e$ ,  $T_e$ ,  $T_i$ , and  $V_i$  on the EISCAT UHF radar data with 1.8 km range steps and 4 s time steps. BAFIM was tuned so that the “effective” time and range resolutions of  $N_e$  are very close to the time and range steps, while resolutions of the other plasma parameters are effectively coarser. Interested readers are referred to Table 1 of Virtanen et al. (2021) for the values of the tuned analysis parameters and their physical meanings. For this particular study, however, we changed the electron density correlation length ( $s^h$ ) and process noise ( $s^f$ ) scaling parameters to 0.1 and  $1.0 \cdot 10^{12} \text{ m}^{-3} \text{ s}^{-1/2}$ , respectively. The 1.8 km resolution was chosen, because it produces better temperature estimates than the 0.9 km resolution, and the change from 0.9 to 1.8 km resolution did not affect results of the subsequent ELSPEC analysis. The raw electron density is first calculated from the same data with 0.9 km range resolution and 4 s time resolution, and then integrated in range to 1.8 km range resolution to match the corresponding resolution of the BAFIM analysis. The alternating code experiment does not provide true backscattered powers, but the raw density is calculated from a short non-zero lag of the ACF.

In order to demonstrate the bias in the raw electron density and its subsequent effect on the energy spectra analysis, we choose for the analysis the expansion phase of the first substorm during which pronounced electron heating was observed. The electron density ( $N_e$ ) and temperature ratio ( $T_e/T_i$ ) fit results obtained from the BAFIM analysis are placed in the first and fourth panels of Figure 3, respectively. The raw electron density ( $N_r$ ) is shown

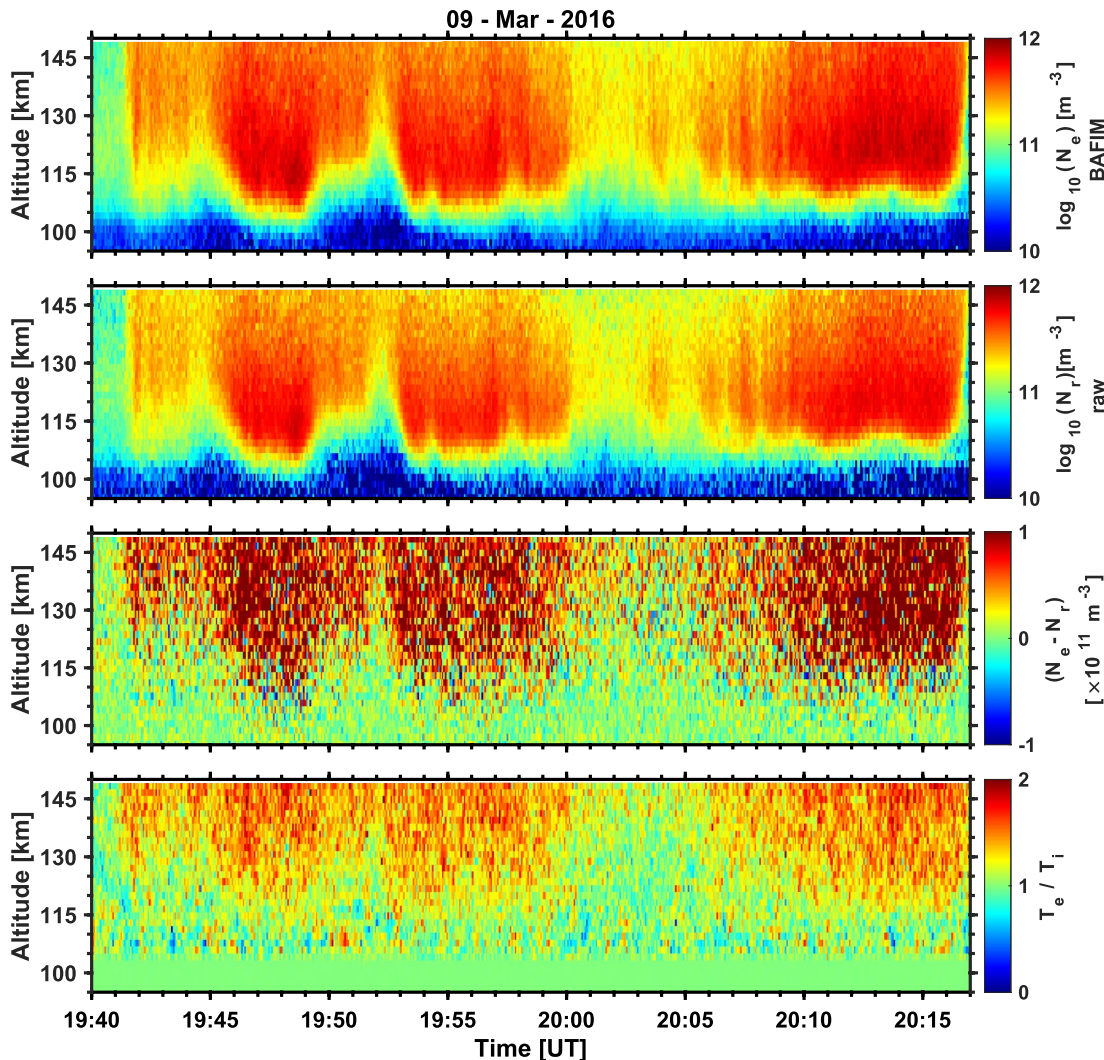


**Figure 3.** Comparison of the raw electron density  $N_r$  and the Bayesian Filtering Module (BAFIM)-fitted density  $N_e$ . Panels from top to bottom: BAFIM  $N_e$ , raw density  $N_r$ , Difference  $N_e - N_r$ , and temperature ratio  $T_e/T_i$  from the BAFIM fit.

in the second panel of the figure. The difference  $N_e - N_r$  is shown in the third panel. As shown in the first and second panels of Figure 3, three intervals of enhanced ionization can be identified from the electron density plots, which are associated to specific auroral features discussed in Section 3.

As shown by the bottom panel of the figure, time intervals with  $T_r > 1$  match with the periods of enhanced ionization. These concurrent enhancements indicate that the energy deposited during the course of precipitation is the cause of the observed electron gas heating. A well established elevation in the electron temperature ( $T_r > 1$ ) can be identified, on average, above about 115 km during all periods of enhanced ionization. In addition,  $T_r$  is shown to increase substantially with altitude to values greater than 1.5 above 130 km during each period of enhanced ionization. Below 103 km we do not fit the temperature ratio, rather we assume  $T_r = 1$ , which is a valid assumption since collision balances the ion and electron temperatures at these altitudes.

The third panel of Figure 3 shows significant differences between the BAFIM electron density and raw electron density estimates during times of electron heating, that is, when  $T_r > 1$ . Substantial difference (of the order of  $10^{11} \text{ m}^{-3}$ ) can be identified down to 115 km altitude during each period of enhanced ionization. The observed differences increase substantially with altitude and reach about 50% close to 150 km altitude. On the other hand, although the ionization enhancements extend down to 100 km altitude, the difference between BAFIM-fitted and raw electron densities is insignificant below 115 km. This is because frequent collisions balance the electron, ion, and neutral temperatures at these altitudes.

#### 4.3. Electron Energy Spectrum Fit With ELSPEC

We use the ELSPEC software (Virtanen et al., 2018) to invert the electron density altitude profiles into differential number flux of the precipitating electrons. ELSPEC solves the electron continuity equation that involves the time derivative of the electron density, the ion production ( $Q$ ) and loss ( $L = \alpha N_e^2$ ) rates:

$$\frac{dN_e}{dt} = Q - \alpha N_e^2. \quad (2)$$

Ion production by mono-energetic electron beams is calculated using the model of Fang et al. (2010), and the ion production by electrons with wide energy spectrum is calculated as a sum of monoenergetic contributions at selected energy bins. The effective recombination coefficient  $\alpha$  as function of ion composition and electron temperature is from Sheehan and St.-Maurice (2004), where the ion composition is from the International Reference Ionosphere (Bilitza et al., 2017) and the electron temperature is from EISCAT ISR measurements. ELSPEC solves the electron density as function of time from the electron continuity Equation 2, assuming that  $\alpha$  and the electron flux remain constant during a radar integration, and iteratively minimizes the difference between the modeled and measured electron density profiles. The fit is performed for a number of different spectrum models in each time step, and the optimal model is selected using the Akaike information criterion (Burnham & Anderson, 2002). The technique is targeted for auroral electrons with energies between 1 and 100 keV, which ionize the atmosphere between 80 and 150 km altitudes.

Originally, ELSPEC used raw electron densities ( $N_r$ ) as input to high-resolution analysis, because the four-parameter fits were not possible with high-resolutions. The electron temperature data needed for the recombination speed calculations was taken from standard GUIDAP fits with 60 s time and a few km range resolutions, and interpolated to the time and range resolutions of the raw electron density. In this study, we use the BAFIM-fitted high-resolution (4 s/1.8 km)  $N_e$  and  $T_e$  as inputs to ELSPEC for the first time. In order to study how much the fitted energy spectra change when the raw electron density  $N_r$  is replaced with the fitted  $N_e$ , we ran the ELSPEC analysis also with the raw density  $N_r$  as input.

#### 4.4. Effect of Electron Heating on Energy Spectrum Fit

We applied the ELSPEC analysis on the raw and BAFIM-fitted electron densities shown in Figure 3 to demonstrate the effect of electron heating on the electron energy spectra fits. This time interval corresponds to the expansion phase of the first substorm during which enhanced electron gas heating was observed for several minutes. Figure 4 shows comparison of the ELSPEC fit results with raw density  $N_r$  and fitted density  $N_e$  as inputs. From top to bottom, the panels are the BAFIM-fitted electron density ( $N_e$ ), the differential energy flux



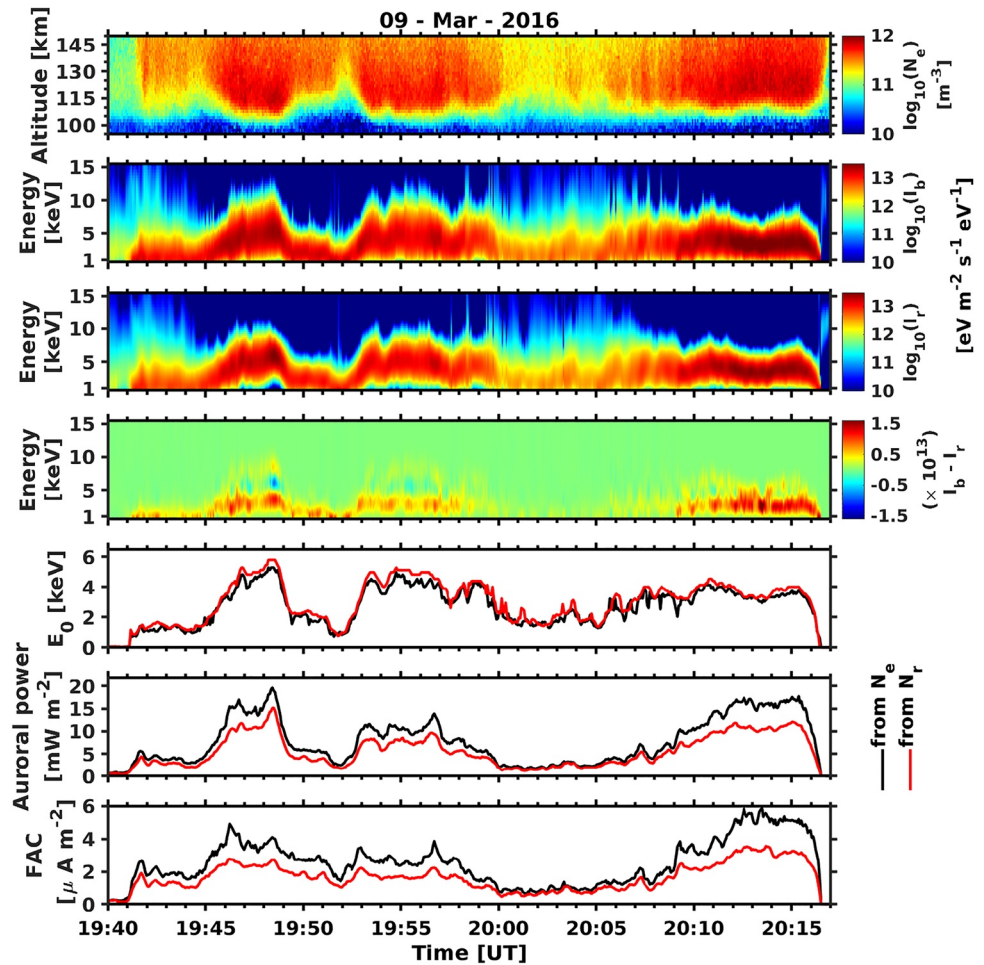


**Figure 4.** Comparison of ELSPEC fit results using raw density  $N_r$  and the Bayesian Filtering Module (BAFIM)-fitted density  $N_e$  as inputs. Panels from top to bottom: The BAFIM-fitted  $N_e$ , the differential electron energy fluxes inverted from the BAFIM-fitted  $N_e$  ( $I_b$ ) and raw density ( $I_r$ ), difference between  $I_b$  and  $I_r$  ( $I_b - I_r$ ), peak energies ( $E_0$ ), auroral powers, and field-aligned currents (FAC). In panels 5–7, the black and red curves correspond to the BAFIM-fitted and raw electron density results, respectively.

inverted from the BAFIM-fitted electron density ( $I_b$ ), the differential energy flux inverted from the raw electron density ( $I_r$ ), the difference between  $I_b$  and  $I_r$  ( $I_b - I_r$ ), peak energy ( $E_0$ ), auroral power, and field-aligned current (FAC). The peak energy is the energy at which the differential energy flux reaches its maximum value. The auroral power, which is equal to the total energy flux, is calculated by integrating the differential energy flux over all energies above 1 keV. The field-aligned current is proportional to the total number flux, which is calculated by integrating the differential number flux. The FAC estimate represents the upward electric current carried by the downward precipitating electrons with energies larger than 1 keV. The ELSPEC FAC estimates are thus merely lower limits for the total FAC, in which the contribution of low-energy electrons could be significant.

Comparing the second and third panels of Figure 4, wider energy distribution is observed in the energy spectra calculated from BAFIM  $N_e$  than in the one obtained from raw density  $N_r$ . Specifically, larger fluxes are observed at lower energies (below about 5 keV) of  $I_b$  than that of  $I_r$ , as shown in the 4th panel of the figure. On the other hand, the peak energies obtained from raw density  $N_r$  slightly exceed those obtained from BAFIM  $N_e$  (5th panel). This is another indication that the energy distribution obtained from BAFIM  $N_e$  tends to have a larger electron flux at its lower energies. The larger flux at lower energies of  $I_b$  account for  $N_e > N_r$  above 115 km altitude, as discussed in Section 4.2.

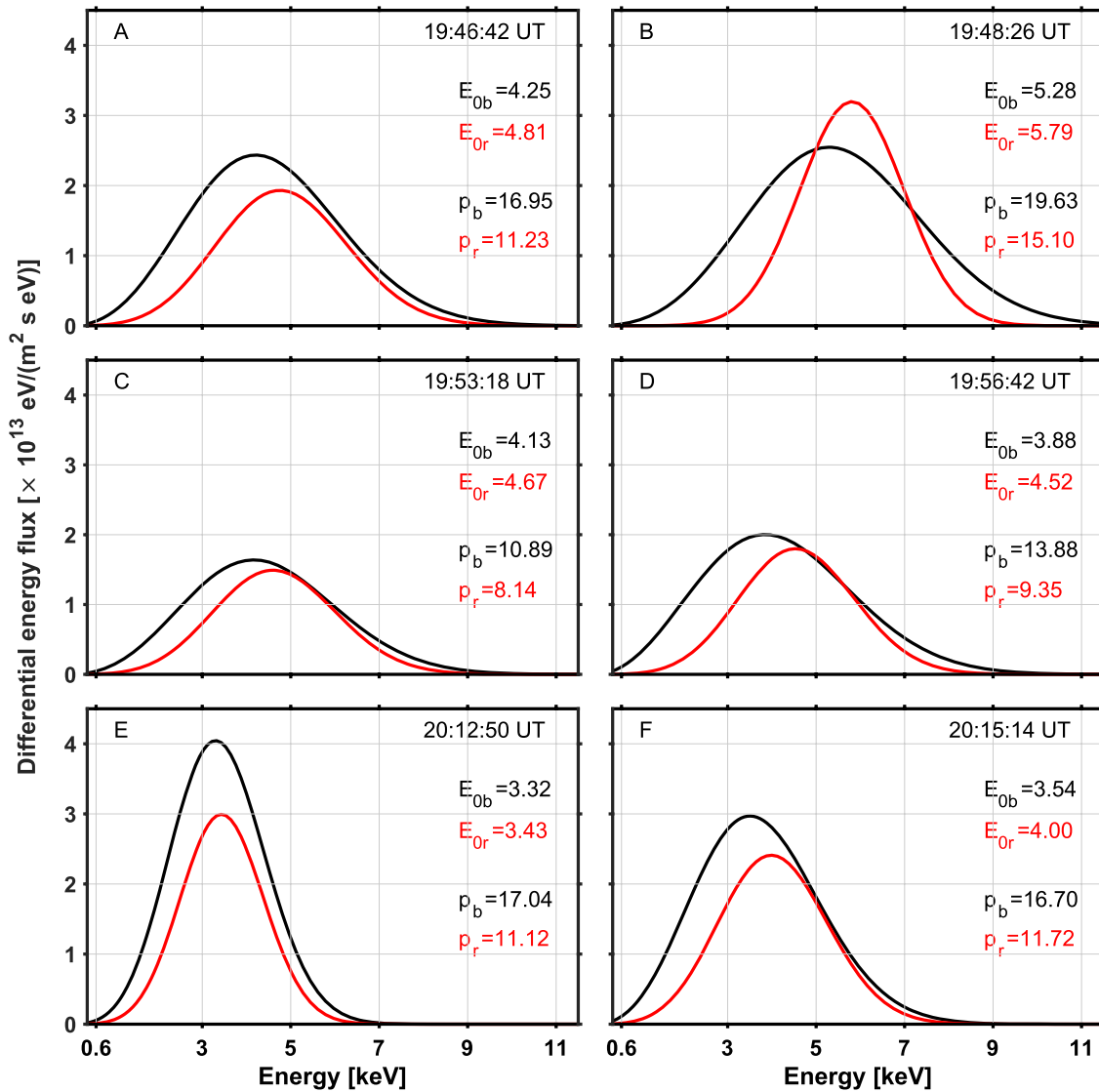


**Figure 5.** Comparison of selected differential energy flux estimates calculated from Bayesian Filtering Module (BAFIM)-fitted electron density  $N_e$  (black) and raw electron density  $N_r$  (red).  $E_{ob}$  and  $P_b$  are the peak energies (in keV) and auroral power estimates (in mWm<sup>-2</sup>) calculated from the BAFIM-fitted  $N_e$ .  $E_{or}$  and  $P_r$  are the corresponding quantities calculated from the raw density  $N_r$ .

The 6th panel of Figure 4 shows a pronounced difference between the auroral power estimates during the first and last periods of enhanced ionization, 19:45–19:48 UT and 20:09–20:16 UT. During both periods, the auroral power calculated from the BAFIM-fitted  $N_e$  exceeds its counterpart calculated from raw density  $N_r$  by about 5 mWm<sup>-2</sup> (50%). For the FAC estimates (7th panel), the difference is observed for longer time intervals, 19:45–19:57 UT and 20:09–20:15 UT, during which larger FAC estimate, by about 2 μAm<sup>-2</sup> (65%), is derived from the fitted electron density than from the raw electron density. In general, the total energy flux and number flux estimates obtained from BAFIM  $N_e$  exceed those obtained from raw density  $N_r$  during each period of enhanced ionization. Detailed distribution of the differences in auroral power and FAC estimates across the entire data is discussed in Section 4.5.

Figure 5 shows line plots of selected differential energy flux estimates derived from the BAFIM-fitted  $N_e$  (black) and raw density  $N_r$  (red). The line plots in panels A–F of the figure show energy spectra of the precipitating electrons that produce the corresponding auroral arcs shown in panels A–F of Figure 2. The peak energies (in keV) and auroral power estimates (in mWm<sup>-2</sup>) at the given time instants are also shown in the figure. All the line plots distinctly demonstrate that the differential energy flux calculated from the BAFIM-fitted  $N_e$  contains larger

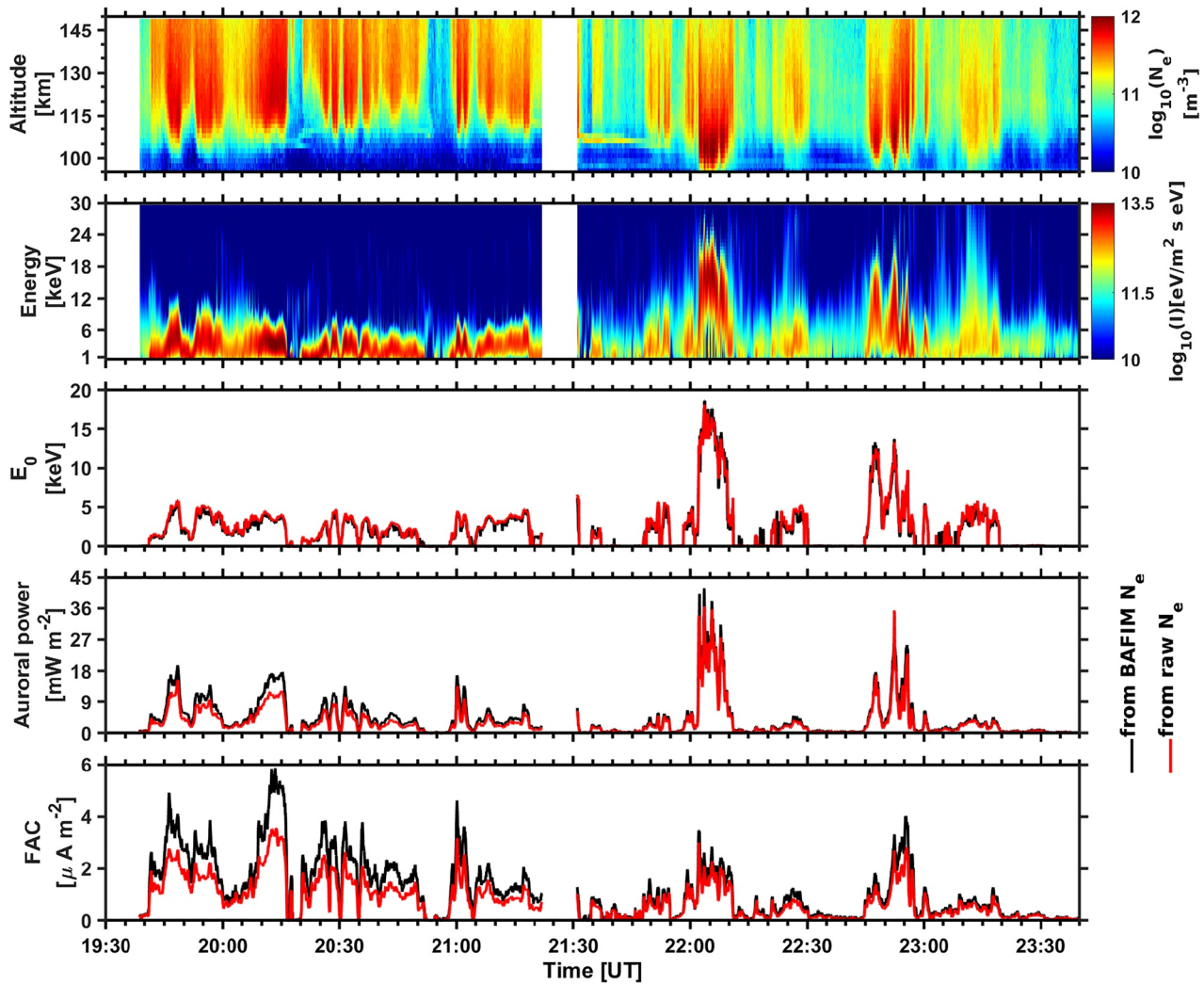


**Figure 6.** ELSPEC fit results during the whole event. Panels from top to bottom: BAFIM-fitted  $N_e$ , differential energy flux, peak energies, auroral powers, and FAC. In panels 3–5, the black and red curves correspond to ELSPEC analysis results using the BAFIM-fitted  $N_e$  and raw density  $N_r$ , respectively.

energy flux below its peak energy than its counterpart calculated from the raw electron density. In addition, the energy spectra obtained from the raw electron density  $N_r$  shows narrower energy distribution as compared to its counterpart calculated from the BAFIM-fitted  $N_e$ .

BAFIM-ELSPEC analysis results in Figure 5 (black curves) indicate that the bright arcs inside the radar beam shown in Figure 2 are produced by precipitating electrons of peak energies between 3 and 5 keV. In addition, the total energy flux of the electrons that powers the arcs lies in the range between 10 and 20  $\text{mWm}^{-2}$ . The 20  $\text{mWm}^{-2}$  auroral power, the largest one here, corresponds to the bright auroral arc observed in the early expansion phase of the first substorm, at about 19:48 UT, as shown in Figure 2.

#### 4.5. Electron Energy Spectra From the Whole Time Interval

Figure 6 shows different parameters derived from the radar data of the entire event that comprises the three substorm activities. In the first and second panels, we have the BAFIM-fitted  $N_e$  and the corresponding differential energy flux results, respectively. The peak energy, auroral power, and FAC estimates are placed in the remaining panels from top to bottom. In panels 3–5, the black and red curves represent parameters derived from the BAFIM-fitted and raw electron density results, respectively.

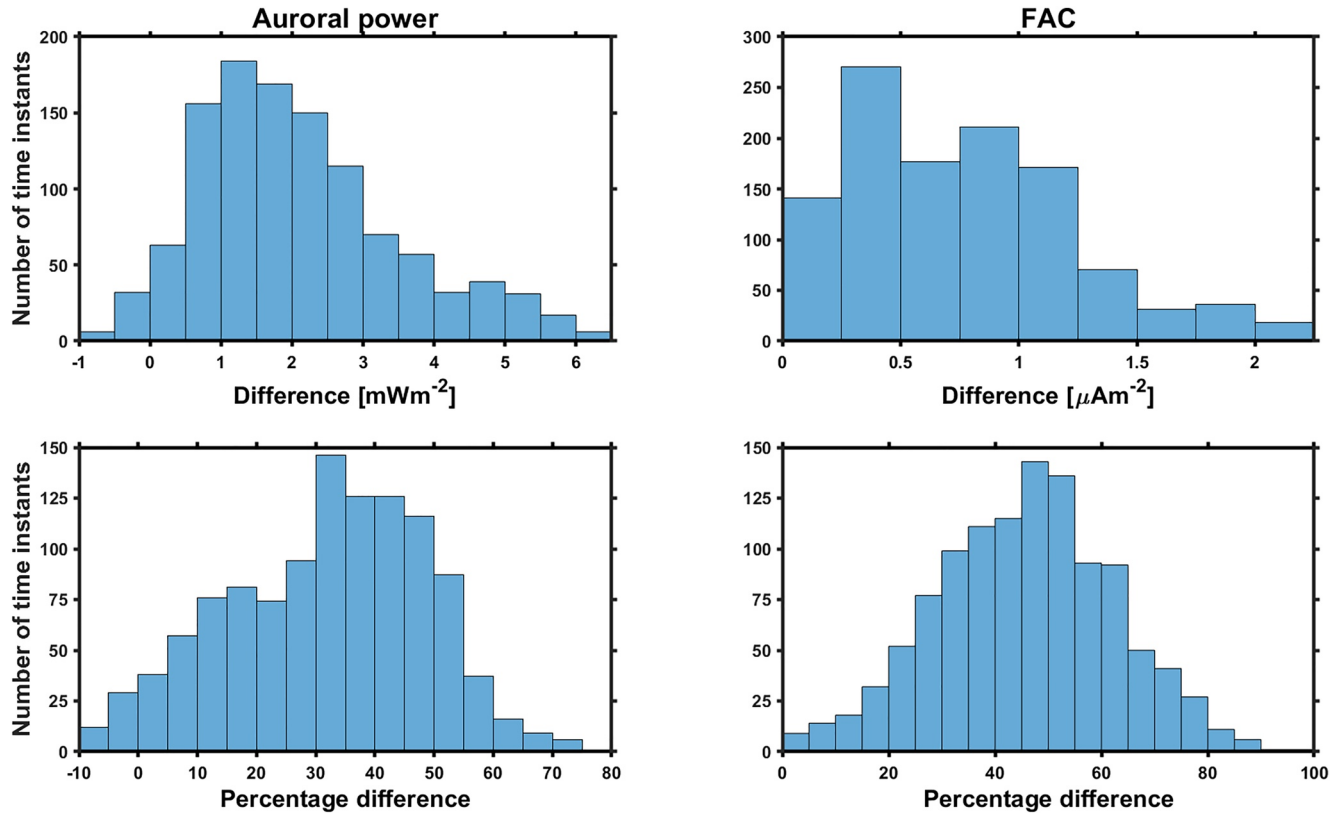


**Figure 7.** Distribution of the absolute and percentage differences in the auroral power (left panels) and field-aligned current (FAC; right panels) estimates.

Several ionization enhancements with different peak altitudes are shown in the electron density plot. Ionization enhancements shown before about 21:30 UT have peak altitudes that lie between 110 and 120 km. Energy distributions of the precipitating electrons that produce these enhancements were peaking between 3 and 5 keV, as shown in the second and third panels. After 21:30 UT, mainly two enhanced ionization periods are shown with lowered peak altitudes in the range between 100 and 106 km. The enhancements are produced by hardening of the precipitating electrons whose energies reach as large as 21 keV, as shown in the second panel of the figure. The largest peak energy and auroral power estimates of the entire event are about 18 keV and  $40 \text{ mWm}^{-2}$ , respectively, corresponding to the bright and large auroral bulge observed in the post-midnight sector during the recovery phase of the second substorm, as illustrated in panel I and J of Figure 2. In general, the large ionization enhancements observed before and after 21:30 UT are produced by flux of electrons whose peak energy lies in the range 3–5 keV and 5–18 keV, respectively. Moreover, several of the auroral structures observed during each substorm event are characterized by inverted-V energy spectra structures. The second panel of the figure shows these structures, for example, in the time intervals 19:45–19:50 UT, 22:01–22:10 UT, and 22:45–23:00 UT, owing to rapid motion of auroral arcs across the radar beam as detailed in Section 3.

The inference from the bottom two panels of Figure 6 is that the auroral power and FAC estimates obtained from the BAFIM-fitted  $N_e$  significantly exceed their counterparts obtained from the raw density  $N_r$  during the first substorm before 21:30 UT. However, during the last two substorm periods after 21:30, the differences become smaller. This is because, before 21:30 UT large flux of lower energy electrons deposit their energy at higher altitudes and heat the electron gas above the ion temperature. Whereas for those periods after 21:30 UT, the electrons become sufficiently energetic and cause enhanced ionization below 115 km altitude, where collisions balance the ion and electron temperatures. Electron temperature was sometimes higher than ion temperature at high altitudes (>120 km) after 21:30 UT, but this has a relatively small effect on the derivation of auroral power and FAC because peaks of the electron density altitude profiles were at lower altitudes.

Figure 7 presents distribution of the actual and percentage difference between the auroral powers (left panel) and FAC (right panel) calculated from  $N_e$  and  $N_r$  data of the whole time interval (4 hr). The differences are calculated



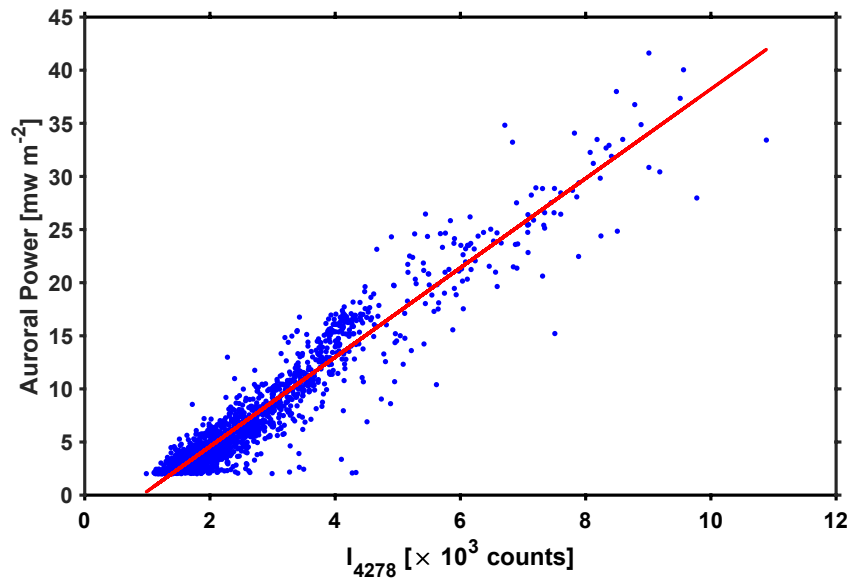


**Figure 8.** Fitting the blue line emission data to the auroral power calculated by ELSPEC using the Bayesian Filtering Module (BAFIM) fitted electron density.

only for time instances at which the auroral power calculated from  $N_e$  is greater than  $3 \text{ mWm}^{-2}$ . The histograms show that the differences between the auroral power estimates peak in the range  $0.5\text{--}2.5 \text{ mWm}^{-2}$  (30%–45%). For the FAC estimates, the peak difference is in the range  $0.25\text{--}0.5 \text{ } \mu\text{Am}^{-2}$  (45%–55%). The largest differences between the auroral power estimates is about 75%. In general, the histograms show that the auroral power and FAC estimates calculated from  $N_e$  typically exceed those from  $N_p$ , but most of the times the difference is smaller than those extreme cases discussed in Section 4.4.

## 5. Comparison to Optical Observations

### 5.1. Auroral Power From Radar and Blue Molecular Band Emission Intensity

We validate our radar analysis results by means of comparing radar observations of auroral power with simultaneous, co-located observation of the blue 427.8 nm emission intensity, utilizing their proportionality relationship. The emission intensity data used in this study is in arbitrary pixel count units without being corrected for dark current leakage in the detectors (Nel, 2019), possible contributions from night time air-glow emission, and atmospheric scattering of light from nearby sources. We subtract the background and scale the emission intensities to the same units with the radar data by means of a linear least squares fit between the auroral power and the blue line emission intensity. The emission intensity used in the linear fit is the median intensity of five pixels found inside the radar beam. Equation 3 and Figure 8 show results of the linear fit between the blue line emission data and auroral power estimates calculated from BAFIM-fitted  $N_e$ .

$$P = 0.0042I_{4278} - 3.8333, \quad (3)$$

where  $P$  is in  $\text{mWm}^{-2}$  and the constant term is attributed to the background data sources in the optical data. Figure 8 demonstrates a very good linear relationship between the 427.8 nm emission intensity and the total energy flux of the precipitating electrons. For this particular event, we calculated a cross-correlation coefficient value of 0.96 between the auroral power and the 427.8 nm emission intensity.

Comparison between the temporal variations of the scaled 427.8 nm emission intensity and the auroral power is shown in the top panel of Figure 9. As shown in the figure, both large-scale and small-scale variations of the 427.8 nm emission intensity match very well with variations in auroral power calculated from radar data. Furthermore, sharp temporal gradients in the emission intensity are captured by the auroral power calculated from the radar data using the BAFIM-fitted electron density. By “sharp gradients” we refer to variations in time scales of

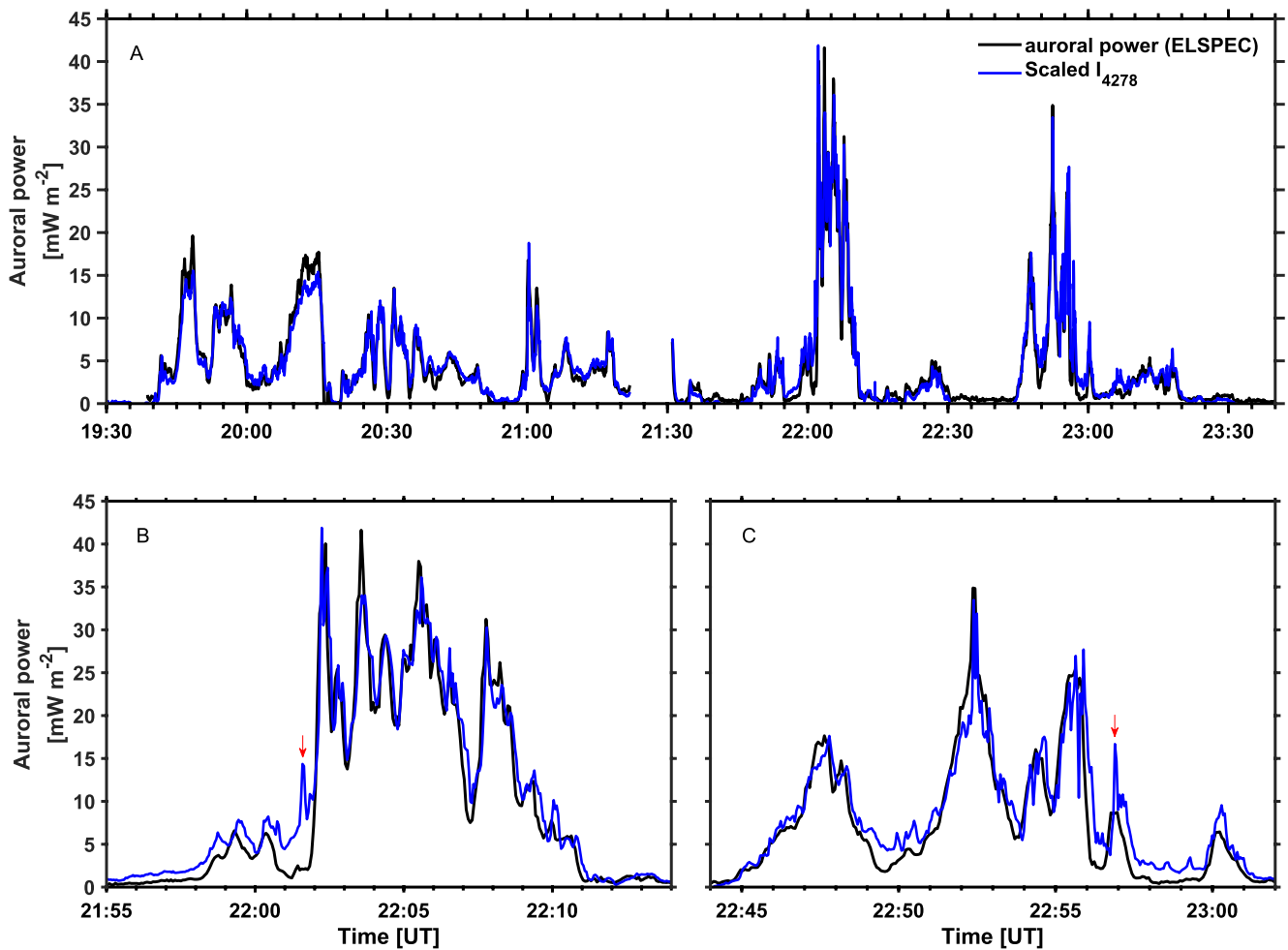


**Figure 9.** Panel (A): Comparing the temporal variations of the auroral power (black) and the scaled emission intensity (blue). Panels (B and C): selected periods from panel (A).

the radar integration (4 s) in this context. Effects of precipitation flux variations during a radar integration are discussed in Section 5.2.

There are some instances when the scaled emission intensity is smaller than the auroral power calculated from the radar data. This happens, for example, between 20:11 and 20:15 UT when the flux of about 1 keV electrons was large. Previous studies have shown that the prompt emission rate of blue photons per unit deposited energy decreases with altitude and characteristic energy of the depositing electrons (Partamies et al., 2004; Rees & Luckey, 1974). As a result, our scaled 427.8 nm emission intensities might be underestimates of the auroral power during these time intervals. Another potential cause of the discrepancy is overestimation of the auroral power by ELSPEC due to ion composition variations. The effect of ion composition variations was studied by Virtanen et al. (2018), who found that the Sodankylä Ion and Neutral Chemistry (SIC) model (Turunen et al., 2016) predicts enhanced and rapidly varying  $O_2^+$  to  $NO^+$  ion ratios during electron precipitation, and ELSPEC analysis with  $O_2^+$  to  $NO^+$  ion ratio taken from the International Reference Ionosphere (Bilitza et al., 2017) produced up to 20% larger auroral powers than the corresponding analysis using SIC ion compositions in an event study.

## 5.2. Effect of Narrow Auroral Structures on ELSPEC Analysis

Figure 9 also shows a few instances when the scaled emission intensity is clearly larger than the auroral power calculated from radar data. For better visualization, selected parts of the comparison graph which contain these

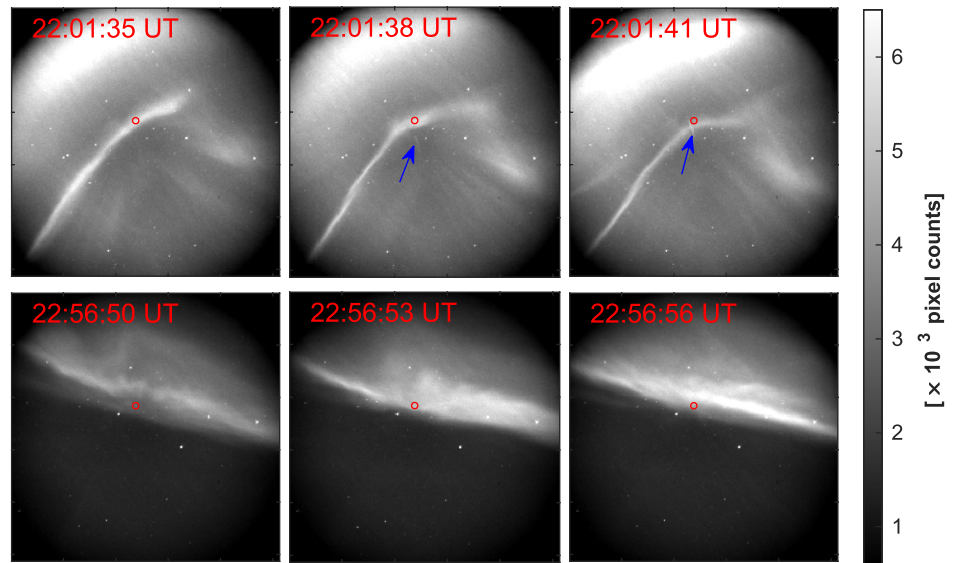


**Figure 10.** Narrow field of view (FoV) auroral images at the given instants of time. The red circle represents the radar beam and the arrows indicate to a passing satellite.

time instants are shown separately in panels B and C of Figure 9. Centered at each time instant, narrow FoV auroral images from three subsequent 3 s exposure times are shown in Figure 10. The first one occurs between 22:01:35 UT and 22:01:41 UT (indicated by a red arrow in panel B of Figure 9) when a thin auroral structure with rapidly varying intensity is within the radar beam, as shown in the top panels of Figure 10. The images indicate that the radar beam is not filled uniformly by the arc before and after 22:01:38 UT. In addition, a satellite crossed the radar beam at 22:01:41, and light reflected from the satellite contributes to the observed emission intensity. The satellite is marked with blue arrows in Figure 10. Panel C of Figure 9 shows the next significant discrepancy at around 22:56:53 UT (indicated by a red arrow), when the equatorward edge of an east-west elongated arc enters the radar beam and returns back within a time scale shorter than the radar integration time, as shown in the bottom panels of Figure 10.

The small-scale structures and rapid variations are a probable reason for the differences in these cases. The comparison between radar and optical data breaks down when the fields of view are not uniformly filled (Lanchester et al., 1997) or when the aurora is more dynamic than the available time resolution. In the radar analysis, violating the implicit assumption of uniform energy flux within the radar beam and during the radar integration time readily leads to underestimation of the total flux. The same effect has been demonstrated by Tuttle et al. (2014) and was discussed also by Dahlgren et al. (2011).

## 6. Discussion and Summary

This study demonstrates for the first time the applicability of a novel combination of two analysis methods (BAFIM and ELSPEC) for estimation of precipitating electron energy spectra, auroral power, and upward FAC from ISR measurements. The unique advantages of this combined analysis is utilization of the fitted electron density, instead of the raw electron density, with high time and range resolutions as input for the ELSPEC analysis. This removes a bias caused by electron heating that may have existed in previous high time resolution ISR observations which have relied on the raw electron density. Accurate electron energy spectra estimates are crucial for studies of small-scale, rapidly varying auroras, and ISRs are currently the best available instruments for such observations.

The BAFIM-ELSPEC analysis method is applied to an auroral event containing three small substorms that occur in the pre-midnight and post-midnight sectors on 9 March 2016. The four-parameter fits of  $N_e$ ,  $T_e$ ,  $T_i$ , and  $V_i$  to the E region EISCAT UHF ISR data were performed with 4 s/1.8 km resolutions by using the BAFIM (Virtanen

et al., 2021). We find that  $N_r$  is systematically smaller than  $N_e$  in the E region when electron precipitation heats the electron gas above the ion temperature. The effect is largest at the top of the E region, where  $N_e$  is up to 50% larger than  $N_r$  above 130 km altitude, but significant differences are also observed down to 115 km.

When the fitted  $N_e$  is used in electron energy spectrum fits with ELSPEC (Virtanen et al., 2018), wider energy spectra and larger total fluxes are produced than in the corresponding analysis with  $N_r$  as input. Larger number fluxes are produced at the low-energy end of the spectra in particular. Auroral power (total energy flux) integrated from the fitted energy spectra is up to 75% larger than the estimates calculated with  $N_r$  as input. However, the distribution of the difference peaks at lower values between 30% and 45%. Similarly, the upward FAC estimate is typically 45%–55% higher when the fitted  $N_e$  is used instead of the raw electron density. These results indicate that previous studies that have relied on the raw electron density may have significantly underestimated the auroral power and upward field-aligned current carried by the precipitating electrons.

Significant differences between the auroral power estimates are observed during the expansion phase of the first substorm which occurred in the pre-midnight sector in connection to flux of precipitating electrons with peak energies between 3 and 5 keV. The differences become insignificant when the precipitating electrons are sufficiently energetic to produce ionization at lower altitudes, in this study below 115 km. This happens, in this study, corresponding to the post-midnight auroral activities during the second and third substorm periods. The auroral power estimates corresponding to observed ionization enhancements during the night of 9 March 2016 were in the range of 3–40 mWm<sup>−2</sup>. These values are in accordance with several other previous studies (Dahlgren et al., 2011; Kaeppler et al., 2015; Stenbaek-Nielsen et al., 1998). The largest auroral power of the night, 40 mWm<sup>−2</sup>, was associated with a bright auroral bulge observed in the post-midnight sector as a result of precipitating electrons with peak energies as large as 18 keV.

The auroral powers calculated using the BAFIM-ELSPEC analysis combination were compared to column intensities of the optical 427.8 nm emission to validate the estimates. A linear correlation between the two were found, and the temporal evolution showed an excellent match. A few significant discrepancies during short time periods were found, but those were shown to correspond to situations when auroral structures narrower than the radar beam move across the beam, or when the electron energy spectrum changes considerably during a radar integration. In these cases, the observed discrepancies indicate that structures narrower than the radar beam and variations in time scales shorter than the radar integration lead to underestimation of the total electron flux in ELSPEC.

Only electrons with energies larger than 1 keV are included in the estimates of auroral power and FAC in this study. ELSPEC cannot reliably estimate electron fluxes at lower energies, because the low-energy electrons produce ionization above 150 km altitude, where plasma convection and concentration of the long-lived O<sup>+</sup> ions may be significant. Ionization by the low-energy electrons can be seen in F region ISR measurements, but it cannot be reliably used for the energy spectra inversion. As a consequence, the FAC estimates of ELSPEC are merely lower limits, because contribution of low-energy electrons to the total FAC could be significant. The auroral power estimates are expected to be less affected, since the energy flux is typically dominated by auroral electrons with energy greater than 1 keV.

Strong electric fields are sometimes known to exist adjacent to auroral arcs in the ionosphere and they typically point toward the arc center (Aikio et al., 2002; Lanchester et al., 1996). In the F region, the corresponding ion drifts take place along the auroral arc, but with decreasing altitude the ion velocity turns more and more in the direction of electric field due to Pedersen mobility in the E region, which means that the plasma in the low-density region outside of the arc may intrude to the more dense plasma inside the arc. This kind of behavior has been observed as an electron density depletion around 125 km altitude by Dahlgren et al. (2011) at the trailing edge of an arc. Such density depletion would be incorrectly interpreted as very fast recombination by ELSPEC. However, in the future, we will be able to measure the 2D horizontal plasma drift pattern in the E and F regions by the EISCAT\_3D radar (McCrea et al., 2015) and take into account the advection term in the continuity equation.

The present work uses 4 s time resolution due to limitations of the BAFIM-GUISDAP software combination. Without this limitation, we should be able to match the time resolution with duration of the alternating code cycle, which is 0.44 s in case of the arc1 experiment. It is also technically possible to run ELSPEC with sub-second resolution data. As a matter of fact, the 0.44 s resolution energy spectra published by Dahlgren et al. (2011) were calculated by a software that was used as a starting point for ELSPEC development.



## Data Availability Statement

EISCAT data are available for download from <https://portal.eiscat.se/schedule/>. The auroral blue line emission intensity data used in this study is available at <https://figshare.com/s/bf5482eb4a1f6bd0fc0a>, and quick-look images for the Watec monochromatic imager (WMI) can be accessed from <http://pc115.seg20.nipr.ac.jp/www/AQVN/index.html>. The image magnetometer network data is available at <https://space.fmi.fi/image/www/index.php?page=userdefined>.

## Acknowledgments

The authors acknowledge the EISCAT Association for the ISR data used in this study. EISCAT is an international association supported by research organisations in China (CRIRP), Finland (SA), Japan (NIPR and ISEE), Norway (NFR), Sweden (VR), and the United Kingdom (UKRI). The authors thank T. Raita, Sodankylä Geophysical Observatory, Finland, for the Kilpisjärvi Pulsation magnetometer data. The authors thank the institutes who maintain the IMAGE Magnetometer Array: Tromsø Geophysical Observatory of UiT the Arctic University of Norway (Norway), Finnish Meteorological Institute (Finland), Institute of Geophysics Polish Academy of Sciences (Poland), GFZ German Research Centre for Geosciences (Germany), Geological Survey of Sweden (Sweden), Swedish Institute of Space Physics (Sweden), Sodankylä Geophysical Observatory of the University of Oulu (Finland), and Polar Geophysical Institute (Russia). The authors would like to thank the World Data Center for Geomagnetism (Kyoto) for the AL index data. This work is supported by the Academy of Finland (301542) and the Kvantum Institute of the University of Oulu.

## References

- Aikio, A. T., Lakkala, T., Kozlovsky, A., & Williams, P. J. S. (2002). Electric fields and currents of stable drifting auroral arcs in the evening sector. *Journal of Geophysical Research*, 107(A12), SIA3-1–SIA3-14. <https://doi.org/10.1029/2001JA009172>
- Baron, M. J. (1977). The Chatanika radar system. In A. Brekke (Ed.), *Radar probing of the auroral plasma* (pp. 103–141). Universitetsforlaget.
- Bilitza, D., Altadill, D., Truhlik, V., Shubin, V., Galkin, I., Reinisch, B., & Huang, X. (2017). International Reference Ionosphere 2016: From ionospheric climate to real-time weather predictions. *Space Weather*, 15(2), 418–429. <https://doi.org/10.1002/2016SW001593>
- Brekke, A., Hall, C., & Hansen, T. L. (1989). Auroral ionospheric conductances during disturbed conditions. *Annales Geophysicae*, 7, 269–280.
- Burnham, K. P., & Anderson, D. R. (2002). *Model selection and multimodel inference* (2nd ed.). Springer.
- Burns, C., Howarth, W., & Hargreaves, J. (1990). High-resolution incoherent scatter radar measurements during electron precipitation events. *Journal of Atmospheric and Terrestrial Physics*, 52(3), 205–218. [https://doi.org/10.1016/0021-9169\(90\)90124-6](https://doi.org/10.1016/0021-9169(90)90124-6)
- Carlson, C. W., Pfaff, R. F., & Watzin, J. G. (1998). The Fast Auroral SnapshoT (FAST) mission. *Geophysical Research Letters*, 25(12), 2013–2016. <https://doi.org/10.1029/98GL01592>
- Dahlgren, H., Gustavsson, B., Lanchester, B. S., Ivchenko, N., Brändström, U., Whiter, D. K., et al. (2011). Energy and flux variations across thin auroral arcs. *Annales Geophysicae*, 29(10), 1699–1712. <https://doi.org/10.5194/angeo-29-1699-2011>
- Dombeck, J., Cattell, C., Prasad, N., Meeker, E., Hanson, E., & McFadden, J. (2018). Identification of auroral electron precipitation mechanism combinations and their relationships to net downgoing energy and number flux. *Journal of Geophysical Research: Space Physics*, 123(12), 10064–10089. <https://doi.org/10.1029/2018JA025749>
- Fang, X., Randall, C. E., Lummerzheim, D., Wang, W., Lu, G., Solomon, S. C., & Frahm, R. A. (2010). Parameterization of monoenergetic electron impact ionization. *Geophysical Research Letters*, 37(22), L22106. <https://doi.org/10.1029/2010GL045406>
- Fujii, R., Nozawa, S., Sato, M., Matuura, N., Ono, T., Brekke, A., et al. (1995). Comparison between electron spectra calculated from EISCAT electron density profiles and those observed by the DMSP satellites. *Journal of Geomagnetism and Geoelectricity*, 47(8), 771–782. <https://doi.org/10.5636/jgg.47.771>
- Hargreaves, J., & Devlin, T. (1990). Morning sector electron precipitation events observed by incoherent scatter radar. *Journal of Atmospheric and Terrestrial Physics*, 52(3), 193–203. [https://doi.org/10.1016/0021-9169\(90\)90123-5](https://doi.org/10.1016/0021-9169(90)90123-5)
- Holt, J. M., Rhoda, D. A., Tetenbaum, D., & van Eyken, A. P. (1992). Optimal analysis of incoherent scatter radar data. *Radio Science*, 27(3), 435–447. <https://doi.org/10.1029/91RS02922>
- Hsu, T.-S., & McPherron, R. L. (2012). A statistical analysis of substorm associated tail activity. *Advances in Space Research*, 50(10), 1317–1343. <https://doi.org/10.1016/j.asr.2012.06.034>
- Hysell, D. L., Rodrigues, F. S., Chau, J. L., & Huba, J. D. (2008). Full profile incoherent scatter analysis at Jicamarca. *Annales Geophysicae*, 26, 59–75. <https://doi.org/10.5194/angeo-26-59-2008>
- Kaeppeler, S. R., Hampton, D. L., Nicolls, M. J., Strømme, A., Solomon, S. C., Hecht, J. H., & Conde, M. G. (2015). An investigation comparing ground-based techniques that quantify auroral electron flux and conductance. *Journal of Geophysical Research: Space Physics*, 120(10), 9038–9056. <https://doi.org/10.1002/2015JA021396>
- Kallio, E. I., Pulkkinen, T. I., Koskinen, H. E. J., Viljanen, A., Slavin, J. A., & Ogilvie, K. (2000). Loading-unloading processes in the nightside ionosphere. *Geophysical Research Letters*, 27(11), 1627–1630. <https://doi.org/10.1029/1999GL003694>
- Kirkwood, S. (1988). *SPECTRUM: A computer algorithm to derive the flux-energy spectrum of precipitating particles from EISCAT electron density profiles*.
- Kirkwood, S., & Eliasson, L. (1990). Energetic particle precipitation in the substorm growth phase measured by EISCAT and Viking. *Journal of Geophysical Research*, 95(A5), 6025–6037. <https://doi.org/10.1029/JA095iA05p06025>
- Kosch, M. J., Honary, F., del Pozo, C. F., Marple, S. R., & Hagfors, T. (2001). High-resolution maps of the characteristic energy of precipitating auroral particles. *Journal of Geophysical Research*, 106(A12), 28925–28937. <https://doi.org/10.1029/2001JA900107>
- Lanchester, B. S., Kaila, K., & McCrea, I. W. (1996). Relationship between large horizontal electric fields and auroral arc elements. *Journal of Geophysical Research*, 101(A3), 5075–5084. <https://doi.org/10.1029/95JA02055>
- Lanchester, B. S., Palmer, J. R., Rees, M. H., Lummerzheim, D., Kaila, K., & Turunen, T. (1994). Energy flux and characteristic energy of an elemental auroral structure. *Geophysical Research Letters*, 21(25), 2789–2792. <https://doi.org/10.1029/94GL01764>
- Lanchester, B. S., Rees, M. H., Lummerzheim, D., Otto, A., Frey, H. U., & Kaila, K. U. (1997). Large fluxes of auroral electrons in filaments of 100 m width. *Journal of Geophysical Research*, 102(A5), 9741–9748. <https://doi.org/10.1029/97JA00231>
- Lehtinen, M. S., & Häggström, I. (1987). A new modulation principle for incoherent scatter measurements. *Radio Science*, 22, 625–634. <https://doi.org/10.1029/RS022i004p00625>
- Lehtinen, M. S., & Huuskonen, A. (1996). General incoherent scatter analysis and GUIDAP. *Journal of Atmospheric and Terrestrial Physics*, 58(1), 435–452. [https://doi.org/10.1016/0021-9169\(95\)00047-X](https://doi.org/10.1016/0021-9169(95)00047-X)
- Lehtinen, M. S., Huuskonen, A., & Pirttilä, J. (1996). First experiences of full-profile analysis with GUIDAP. *Annales Geophysicae*, 14, 1487–1495. <https://doi.org/10.1007/s00585-996-1487-3>
- McCrea, I., Aikio, A., Alfonsi, L., Belova, E., Buchert, S., Ciliverd, M., et al. (2015). The science case for the EISCAT\_3D radar. *Progress in Earth and Planetary Science*, 2(1), 21. <https://doi.org/10.1186/s40645-015-0051-8>
- McPherron, R. L. (2005). Magnetic pulsations: Their sources and relation to solar wind and geomagnetic activity. *Surveys in Geophysics*, 26(5), 545–592. <https://doi.org/10.1007/s10712-005-1758-7>
- Mishin, V. V., Tsegmed, B., Klivanova, Y. Y., & Kurikalo, M. A. (2020). Burst geomagnetic pulsations as indicators of substorm expansion onsets during storms. *Journal of Geophysical Research: Space Physics*, 125(10), e2020JA028521. <https://doi.org/10.1029/2020JA028521>

- Nel, A. E. (2019). *Novel radar and optical observations of black auroras in the upper atmosphere* (Doctoral dissertation). North-West University. Retrieved from <https://repository.nwu.ac.za/handle/10394/35266>
- Nel, A. E., Kosch, M. J., Whiter, D., Gustavsson, B., & Aslaksen, T. (2021). A new auroral phenomenon, the anti-black aurora. *Scientific Reports*, 11(1), 1829. <https://doi.org/10.1038/s41598-021-81363-9>
- Newell, T., Sotirelis, T., & Wing, S. (2009). Diffuse, monoenergetic, and broadband aurora: The global precipitation budget. *Journal of Geophysical Research*, 114(A9). <https://doi.org/10.1029/2009JA014326>
- Nose, M., Iyemori, T., Sugiura, M., & Kamei, T. (2015). *AE index*. WDC for Geomagnetism. <https://doi.org/10.17593/15031-54800>
- Ogawa, Y., Tanaka, Y., Kadokura, A., Hosokawa, K., Ebihara, Y., Motoba, T., et al. (2020). Development of low-cost multi-wavelength imager system for studies of aurora and airglow. *Polar Science*, 23, 100501. <https://doi.org/10.1016/j.polar.2019.100501>
- Olson, J. V. (1999). Pi2 pulsations and substorm onsets: A review. *Journal of Geophysical Research*, 104(A8), 17499–17520. <https://doi.org/10.1029/1999JA900086>
- Omholt, A. (1971). The electron aurora: Main characteristics and luminosity. In *Physics and chemistry in space* (pp. 24–46). Springer Berlin Heidelberg. [https://doi.org/10.1007/978-3-642-46269-6\\_2](https://doi.org/10.1007/978-3-642-46269-6_2)
- Osepian, A., & Kirkwood, S. (1996). High-energy electron fluxes derived from EISCAT electron density profiles. *Journal of Atmospheric and Terrestrial Physics*, 58(1), 479–487. [https://doi.org/10.1016/0021-9169\(95\)00050-X](https://doi.org/10.1016/0021-9169(95)00050-X)
- Partamies, N., Janhunen, P., Kauristie, K., Mäkinen, S., & Sergienko, T. (2004). Testing an inversion method for estimating electron energy fluxes from all-sky camera images. *Annales Geophysicae*, 22(6), 1961–1971. <https://doi.org/10.5194/angeo-22-1961-2004>
- Raita, T., & University of Oulu. (2022). *Horizontal power spectrum of the Finnish pulsation magnetometer data from kilpisjärvi on 9.3.2016*. University of Oulu, Sodankylä Geophysical Observatory. <https://doi.org/10.23729/d080ce43-e097-4f5d-970d-1f59f28c8517>
- Rees, M. H. (1963). Auroral ionization and excitation by incident energetic electrons. *Planetary and Space Science*, 11(10), 1209–1218. [https://doi.org/10.1016/0032-0633\(63\)90252-6](https://doi.org/10.1016/0032-0633(63)90252-6)
- Rees, M. H., & Luckey, D. (1974). Auroral electron energy derived from ratio of spectroscopic emissions I. Model computations. *Journal of Geophysical Research*, 79(34), 5181–5186. <https://doi.org/10.1029/JA079i034p05181>
- Saito, T. (1969). Geomagnetic pulsations. *Space Science Review*, 10(3), 319–412. <https://doi.org/10.1007/BF00203620>
- Sakurai, T., & Saito, T. (1976). Magnetic pulsation Pi2 and substorm onset. *Planetary and Space Science*, 24(6), 573–575. [https://doi.org/10.1016/0032-0633\(76\)90135-5](https://doi.org/10.1016/0032-0633(76)90135-5)
- Semeter, J., & Kamalabadi, F. (2005). Determination of primary electron spectra from incoherent scatter radar measurements of the auroral E region. *Radio Science*, 40(2). <https://doi.org/10.1029/2004RS003042>
- Sheehan, C. H., & St.-Maurice, J.-P. (2004). Dissociative recombination of N<sub>2</sub><sup>+</sup>, O<sub>2</sub><sup>+</sup>, and NO<sup>+</sup>: Rate coefficients for ground state and vibrationally excited ions. *Journal of Geophysical Research*, 109(A3). <https://doi.org/10.1029/2003JA010132>
- Simon Wedlund, C., Lamy, H., Gustavsson, B., Sergienko, T., & Brändström, U. (2013). Estimating energy spectra of electron precipitation above auroral arcs from ground-based observations with radar and optics. *Journal of Geophysical Research: Space Physics*, 118(6), 3672–3691. <https://doi.org/10.1002/jgra.50347>
- Stenbaek-Nielsen, H. C., Hallinan, T. J., Osborne, D. L., Kimball, J., Chaston, C., McFadden, J., et al. (1998). Aircraft observations conjugate to FAST: Auroral arc thicknesses. *Geophysical Research Letters*, 25(12), 2073–2076. <https://doi.org/10.1029/98GL01058>
- Strickland, D. J., Hecht, J. H., Christensen, A. B., & Kelly, J. (1994). Relationship between energy flux Q and mean energy E of auroral electron spectra based on radar data from the 1987 CEDAR campaign at Søndre Stromfjord, Greenland. *Journal of Geophysical Research*, 99(A10), 19467–19473. <https://doi.org/10.1029/94JA01901>
- Strickland, D. J., Meier, R. R., Hecht, J. H., & Christensen, A. B. (1989). Deducing composition and incident electron spectra from ground-based auroral optical measurements: Theory and model results. *Journal of Geophysical Research*, 94(A10), 13527. <https://doi.org/10.1029/ja094ia10p13527>
- Tanskanen, E. I. (2009). A comprehensive high-throughput analysis of substorms observed by IMAGE magnetometer network: Years 1993–2003 examined. *Journal of Geophysical Research*, 114(A5). <https://doi.org/10.1029/2008JA013682>
- Turunen, E., Kero, A., Verronen, P. T., Miyoshi, Y., Oyama, S.-I., & Saito, S. (2016). Mesospheric ozone destruction by high-energy electron precipitation associated with pulsating aurora. *Journal of Geophysical Research: Atmospheres*, 121, 11852–11861. <https://doi.org/10.1002/2016JD025015>
- Tuttle, S., Gustavsson, B., & Lanchester, B. (2014). Temporal and spatial evolution of auroral electron energy spectra in a region surrounding the magnetic zenith. *Journal of Geophysical Research: Space Physics*, 119(3), 2318–2327. <https://doi.org/10.1002/2013JA019627>
- Virtanen, I. I., Gustavsson, B., Aikio, A., Kero, A., Asamura, K., & Ogawa, Y. (2018). Electron energy spectrum and auroral power estimation from incoherent scatter radar measurements. *Journal of Geophysical Research: Space Physics*, 123(8), 6865–6887. <https://doi.org/10.1029/2018JA025636>
- Virtanen, I. I., Tesfaw, H. W., Roininen, L., Lasanen, S., & Aikio, A. (2021). Bayesian filtering in incoherent scatter plasma parameter fits. *Journal of Geophysical Research: Space Physics*, 126(3), e2020JA028700. <https://doi.org/10.1029/2020JA028700>
- Vondrak, R. R., & Baron, M. J. (1977). A method of obtaining the energy distribution of auroral electrons from incoherent scatter radar measurements. In A. Brekke (Ed.), *Radar probing of the auroral plasma* (pp. 315–330). Universitetsforlaget.
- Wickwar, V. B., Lathuillere, C., Kofman, W., & Lejeune, G. (1981). Elevated electron temperatures in the auroral E layer measured with the Chatanika radar. *Journal of Geophysical Research*, 86(A6), 4721–4730. <https://doi.org/10.1029/JA086iA06p04721>